Visible Light-Illuminated Gold Nanohole Arrays With Tunable On-Chip Plasmonic Sensing Properties

Jianye GUANG[1,3], Mengdi LU[1,2*], Rui LI[2], Chen WANG[3], Ming LIN[2], Ruizhi FAN[2], and Wei PENG[2]

[1]*Cancer Hospital, Dalian University of Technology, Shenyang 110042, China*

[2]*School of Physics, Dalian University of Technology, Dalian 116024, China*

[3]*School of Optoelectronic Engineering and Instrumentation Science, Dalian University of Technology, Dalian 116024, China*

[*]Corresponding author: Mengdi LU E-mail: mdlu@dlut.edu.cn

Abstract: Since the discovery of the extraordinary optical transmission phenomenon, nanohole arrays have attracted much attention and been widely applied in sensing. However, their typical fabrication process, utilizing photolithographic top-down manufacturing technologies, has intrinsic drawbacks including the high costs, time consumption, small footprint, and low throughput. This study presented a low-cost, high-throughput, and scalable method for fabricating centimeter-scale ($1\times2\,cm^2$) nanohole arrays using the improved nanosphere lithography. The large-scale close-packed polystyrene monolayers obtained by the hemispherical-depression-assisted self-assembly method were employed as colloidal masks for the nanosphere lithography, and the nanohole diameter was tuned from 233 nm to 346 nm with a fixed period of 420 nm via plasma etching. The optical properties and sensing performance of the nanohole arrays were investigated, and two transmission dips were observed due to the resonant coupling of plasmonic modes. Both dips were found to be sensitive to the surrounding environment, and the maximum bulk refractive index sensitivity was up to 162.1 nm/RIU with a 233 nm hole diameter. This study offered a promising approach for fabricating large-scale highly ordered nanohole arrays with various periods and nanohole diameters that could be used for the development of low-cost and high-throughput on-chip plasmonic sensors.

Keywords: Plasmonic sensor; nanohole arrays; monolayer; nanosphere lithography; extraordinary optical transmission

Citation: Jianye GUANG, Mengdi LU, Rui LI, Chen WANG, Ming LIN, Ruizhi FAN, *et al.*, "Visible Light-Illuminated Gold Nanohole Arrays With Tunable On-Chip Plasmonic Sensing Properties," *Photonic Sensors*, 2024, 14(3): 240311.

1. Introduction

In recent years, there has been significant progress in the theoretical research and practical applications of plasmonic nanostructures, including clinical medicine, environmental monitoring, photocatalysis, imaging, food safety, and solar energy [1–6]. Plasmonic nanostructures possess multiple tunable properties, such as light absorption, structural color, and electrical characteristics [7]. Additionally, plasmonic nanostructured sensors have excellent near-field localization capacities and can be directly excited by spatial light without the complex and bulky optical prism system, making

Received: 23 August 2023 / Revised: 4 January 2024

DOI: 10.1007/s13320-024-0717-1
Article type: Regular

them widely applicable in biochemical molecule detection, including heavy metal ions [8], protein biomarkers [9], deoxyribonucleic acid (DNA) [10], ribonucleic acid (RNA) [11], and pesticide residues [12]. With the development of advanced materials and design simulations, multiple trials have been conducted on the topography and materials of these nanostructures to enhance their plasmonic properties for sensing. Up to now, plasmonic nanostructured sensors based on nanoparticles [13, 14], nanoholes [15, 16], nanodisks [17, 18], nanorings [19, 20], nanocrescents [21, 22], nanocubes [23], and related derivative structures [24] have been reported. Among these, nanohole arrays have attracted significant interest due to the discovery of the extraordinary optical transmission (EOT) phenomenon [25], where the transmitted light passing through the metallic nanohole arrays displays a higher intensity which conflicts with the standard aperture theory. Besides, the metallic nanohole arrays are sensitive to the refractive index (RI) changes of the surrounding medium due to the joint action of localized surface plasmon (LSP) resonances and surface plasmon polariton (SPP) modes [26]. Relying on these beneficial characteristics, nanohole arrays hold the great promise as an ideal plasmonic sensing platform.

Until now, numerous efforts have been conducted to improve the sensing performance of nanohole arrays through modifications of their structural parameters and the fabrication of novel nanohole arrays. Masson *et al*. [27], for example, conducted a thorough investigation on the optical and analytical properties of gold and silver nanohole arrays with a fixed period of 420 nm and various hole sizes. They concluded that optimizing the metal composition and hole diameter could enhance these properties. With further expansion of studies on mechanisms, it was found that the transmission efficiency was closely linked to the RI of the substrate [28]. Ruan *et al*. [29] produced large-scale, high-uniformity, freestanding gold nanofilms with nanohole arrays supported by a hollow substrate structure. They achieved a high bulk RI sensitivity which was double that of a silicon-based counterpart nanohole array. Moreover, various novel nanostructures based on nanohole arrays have been reported. Wang *et al*. [30] suggested a dual-mode nucleic acid sensor that employed a tetrahedral-DNA-probes-modified silver nanorod-covered silver nanohole array for surface-enhanced Raman scattering (SERS) and surface plasmon resonance (SPR). The SERS and SPR signals were successfully enhanced by 10 times and 4 times, respectively, using the DNA supersandwich strategy. Ai *et al*. [31] introduced an elliptical nanohole array based sensor that optimized the sensitivity, figure of merit, and relative sensitivity up to 775 nm/RIU, 705/RIU, and 70.23%, respectively, using the differential polarization transmission spectra. However, the key prerequisite for realizing all these efforts is the fabrication of large-scale and high-periodicity nanohole arrays.

To date, the majority of nanohole array fabrication methods rely on photolithographic top-down manufacturing, such as the electron-beam lithography (EBL), focused ion beam (FIB) milling, and photolithography [32, 33]. While these techniques offer the high precision, repeatability, and ability to manufacture complex structures, they suffer from substantial limitations, such as the expensive equipment, low throughput, long production time, and small footprint, which make them unsuitable for large-scale manufacturing and seriously limit their practical applications. To address these limitations, the nanosphere lithography (NSL) has been proposed as a low-cost, high-yield, simple, and practical method for fabricating large-scale ordered nanohole arrays by using 2-dimensional (2D) colloidal monolayers as templates [34–36]. The preparation of templates is a key factor in the NSL, and among various strategies for obtaining high-periodicity 2D colloidal

monolayers at a large scale, self-assembling nanospheres on the liquid-air interface are considered to be the most promising and effective method. However, the monolayers prepared through this method may contain multiple defects that can affect the morphology of the structure subsequently fabricated by the NSL. Despite many optimized solutions [37–39] have been reported to address this issue, the effect is limited since the fundamental causes are not eliminated, i.e., the subaquatic nanospheres [40].

Herein, we fabricated high-ordered nanohole arrays through the hemispherical-depression-assisted self-assembly method at the liquid-air interface in combination with subsequent plasma etching processes. The subaquatic nanospheres were substantially eliminated, and the nanohole arrays with a fixed period of 420 nm and various nanohole diameters ranging from 233 nm to 346 nm were obtained. The nanohole arrays serving as plasmonic sensing elements were manufactured on BK7 glass substrates with a large area of $1\times2\,cm^2$. The hole diameter was accurately controlled by adjusting the etching duration. Furthermore, the optical properties and sensing performances of nanohole arrays were experimentally investigated considering the hole diameter. All the nanohole arrays displayed two transmission dips in the spectra, which were sensitive to the surrounding environment. The bulk RI sensitivity could reach up to 162.1 nm/RIU with a nanohole diameter of 233 nm. Our experimental results were in line with numerical simulation predictions. Overall, we proposed meliorative techniques that enabled the cost-effective and rapid preparation of large-scale and high-ordered nanohole arrays with various nanohole sizes, demonstrating the capability and potential of the arrays as on-chip plasmonic sensors.

2. Experimental section

2.1 Materials

The deionized water used in all experiments was ultrapure (18.25 MΩ·cm) obtained from a WP-30L water purification system (Beijing KWF Sci-Tech Development). Monodisperse polystyrene (PS) nanospheres with a uniform diameter of 420 nm, available commercially, were purchased from Nanjing Janus New-Materials. Chemicals such as ethanol, acetone, concentrated sulfuric acid (98%), hydrogen peroxide (30%), and sodium chloride were acquired from Beijing Chemical Works, whereas sodium dodecyl sulfate (SDS) was obtained from Sigma-Aldrich. Microliter syringes were purchased from Shanghai Gaoge Industry Trade, and the silicon wafer with a thickness of 600 μm was obtained from Suzhou Crystal Silicon Electronic Technology. Additionally, BK7 glass slides ($1\times2\,cm^2$) were purchased from Beijing Yongxing Perception Information Technology, and gold powder for vapor deposition was obtained from Beijing Hezong Tianqi New Material Technology. All reagents were analytically graded and used without further purification.

2.2 Template preparation for the NSL

The templates for the NSL were fabricated by the hemispherical-depression-assisted self-assembly of PS nanospheres at the air-water interface, as described in our previous work [41]. In brief, the BK7 glass slides ($1\times2\,cm^2$) and silicon slide ($4\times10\,cm^2$) were thoroughly cleaned with acetone, ethanol, and ultrapure water in an ultrasonic bath for 15 min and then immersed in the piranha solution (98% H_2SO_4:30% H_2O_2=3:1, v/v. Extremely dangerous! Be careful!) for 30 min to introduce hydroxyl groups (OH) and modify the surface with negative charges [42]. Next, an appropriate amount of the SDS surfactant was added to water to reduce the surface tension gradient [43] followed by injecting the PS nanosphere suspension (5 wt% PS nanospheres:ethanol=1:1, v/v) at a constant velocity of 0.4 μL/s along the silicon slide, which was partly immersed and tilted at a 40° angle on the edge of a glass beaker filled with ultrapure water. With the

continued injection of suspension, the water surface would be bent downward along the slide due to the viscous force induced by the velocity gradient [44], forming a hemispherical depression at the water-silicon-air boundary. By utilizing the resistance of the depression, the PS nanospheres would be self-assembled directly into a large-scale monolayer upon reaching the boundary.

After the self-assembly process, the monolayer was transferred onto BK7 substrates via the vertical lifting method. Initially, the pretreated BK7 glass slides were wholly submerged in water, and the edge of the monolayer was secured in contact with the slide. Subsequently, the slides were lifted at a constant speed to successfully transfer the monolayer onto the slide. The proposed methods of hemispherical-depression-assisted self-assembly of PS nanospheres at the air-water interface and vertical lifting gave rise to high-quality colloidal masks.

2.3 Nanohole arrays fabrication and morphology modulation

Evaporating metal in the geometric gap of the mask can result in a periodic array whose periodicity is determined by the diameter of the PS nanosphere. To create the array, a 75 nm-thick gold film was deposited on the template using a resistance thermal evaporator from Shenyang Kecheng Vacuum Technology Co., Ltd. The evaporation rate was set at around 0.2 Å/s to minimize the roughness and enhance the adhesion of gold film contemporaneously. The sample stage was rotated at a speed of 20 rpm during the deposition process, and the vacuum level inside the chamber was maintained at 5×10^{-6} Torr. After deposition, the gold-coated PS nanosphere monolayer was removed by sonication in the tetrahydrofuran solution and ultrapure water each for 5 min. The substrate was then treated with oxygen plasma for 2 min to get rid of any remaining SDS and polystyrene residues on the surface. This manufacturing strategy yielded hexagonal gold triangular arrays supported by glass, with periods that depended on the size of PS nanospheres.

As for the morphology modulation, an oxygen-plasma cleaning device (HM-Plasma2L, Changzhou Hongming Instrument Technology) with the O_2 flow rate of 120 sccm (chamber pressure: 1 Pa) and radio frequency (RF) power of 50 W was employed to regulate the diameter of PS nanospheres without destroying their shape. To ensure the consistency and uniformity, we etched only one slide at a fixed position directly below the center of the electrode plate each time. The diameter of PS nanospheres was adjusted by changing the etching duration (30 s, 60 s, 90 s, 120 s, 150 s, 180 s, 210 s, and 240 s). After metal evaporation and mask removal under the same experimental condition as unetched masks, we obtained highly ordered gold nanohole arrays with various diameters and the fixed period.

2.4 Characterization and measurement

Surface morphologies of the gold nanohole arrays were investigated using the field-emission scanning electron microscopy (SEM, TESCAN MIRA LMS). A halogen light source (HL2000, Ocean Optics, Inc.) emitting light in the range of 300 nm to 2 000 nm was employed to illuminate the arrays. The transmission spectra were recorded via a fiber optic spectrometer (HR4000, Ocean Optics, Inc.) that ranged from 400 nm to 1 100 nm. To acquire and process the experimental data in real time, a home-written Labview program was utilized, with an integration time set to 50 ms and 20 spectra averaged per second.

2.5 Fluidic system

The fluidic system was manufactured through the injection molding of polydimethylsiloxane (PDMS) into a stainless steel template. The flow cell was designed to include two identical channels, each with two narrow slits (5 mm long, 1.2 mm wide, and 1.2 mm high) serving as the sample solution inlet/outlet and a rectangular groove (7.5 mm long, 5 mm wide, and 1.5 mm high) between them serving

as the test area. The slits were made by drilling through the PDMS tube. The fabricated nanohole arrays were then fixed to a four-layer structure composed of the polymethyl methacrylate (PMMA), the nanohole substrate, the PDMS fluidic cell, and another layer of PMMA. Sodium chloride (NaCl) solutions with varying RIs of 1.332, 1.349, 1.358, 1.368, and 1.378, which were determined by an Abbe refractometer, were used as sample solutions. Sample solutions were injected using a peristaltic pump at a constant flow rate of 3 ml/min.

2.6 Simulation

The spectra and electromagnetic fields of a hexagonal gold nanohole array were analyzed using the finite-difference time-domain (FDTD) method with the FDTD Solutions software from Lumerical. The array, which was 233 nm in diameter and 420 nm in periodicity, was situated on a 75 nm gold film that was deposited onto a BK7 glass slide. The simulation unit cell was set to contain only one period of the array, consisting of one hole at the center, four quarter holes at the corners in the *x*-*y* plane, and the sufficient space for a light source and monitors in the *x*-*z* plane. The boundary conditions were set as periodic in the *x* and *y* directions and perfectly matched layers (PML) in the *z* direction. The permittivity of Au was based on the Johnson and Christy model [45]. A plane wave ranging from 400 nm to 1 000 nm was incident normally on the nanohole array from the gold side. The electric field was polarized in the *x* direction (TM polarization) and the magnetic field was considered as unity along the *z* axis. Five monitors were placed separately at 675 nm and 75 nm above the BK7 glass, 0 nm and 500 nm below the array in the *x*-*y* plane, and the orthogonal plane crossing the gold film to measure distributions of electromagnetic fields and transmission spectra. The grid sizes in the *x*, *y*, and *z* directions were all set to 2 nm, 2 nm, and 1 nm, respectively, and the time steps were set to 1 000 fs to satisfy the Courant stability criterion [46]. Besides, the medium upon and among the nanoholes was RI liquids (n=1.33–1.37) or air (n=1), while the medium below the array was BK7 glass (n=1.52).

3. Results and discussion

3.1 Fabrication of gold nanohole arrays

In this work, the main improvement of the proposed NSL method was that we employed the low-cost oxygen plasma cleaner to etch the nanospheres. The aim of this work was to verify the effectiveness and feasibility of this etching method. Therefore, we only considered the effect of the hole size in this manuscript which was directly related to the etching process, fixed the period as 420 nm, and employed gold as the structural composition. Densely packed gold nanohole arrays were fabricated through an improved NSL method utilizing hexagonal close-packed PS monolayers as masks. The fabrication procedure of the nanohole arrays is outlined in Fig. 1, which also shows SEM images for each step. To begin, a PS monolayer was self-assembled on the air-water interface with the aid of a hemispherical depression and subsequently transferred to BK7 slides by vertical lifting. The SEM image in inset (i) illustrates the hexagonal-packed PS nanospheres on the BK7 slide without any defects. The monolayer was then etched to a non-close-packed state, followed by thermal resistance evaporation of a 75 nm thick gold film. It should be noted that previous studies utilizing the NSL method typically employed the expensive and complicated equipment, such as reactive ion etching (RIE) or inductively coupled plasma etching (ICP) for the etching process. Although the consistency and homogeneity of these etching methods are relatively high, the expensive equipment and complicated operations limit their practical applications. In this case, we innovatively used a low-cost oxygen plasma cleaner for the etching of nanospheres. Compared with RIE or ICP, the orientation of oxygen plasma etching is poor. To

ensure the good consistency and uniformity of etching, we strictly controlled the etching conditions, including the temperature, sample position, and operation process. Here, we employed the multi-round etching method to control the temperature, i.e., we first performed the etching for 30 s, then stopped the etching, maintained the system status for 2 min to achieve cooling, and then repeated the process until the desired etch duration was achieved. The SEM image in inset (ii) shows the successful reduction of the nanosphere diameter (with an etching duration of 120 s) without destroying the shape and alignment. Finally, the nanospheres coated with the gold film were removed through sonication in the tetrahydrofuran solution, as depicted in inset (iii), resulting in a hexagonal nanohole array on the slide. The period and size of nanoholes could be precisely tuned by using nanospheres of different diameters as masks and adjusting the etching durations, respectively. Although the monolayers used as masks may contain defects, the versatility, ease of operation, timesaving, and capability of manufacturing large-area structures at low cost using the simple equipment while simultaneously maintaining good control of structural parameters make the process potentially suitable for mass-production of plasmonic sensors.

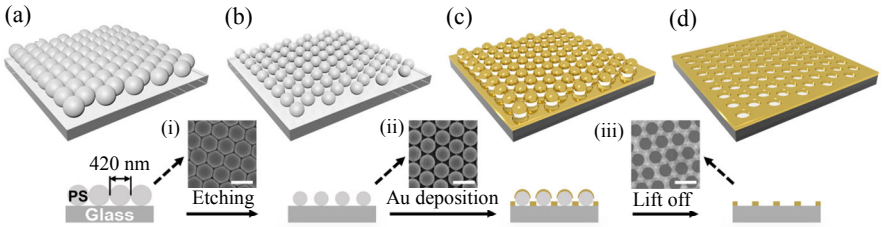

Fig. 1 Schematic of the fabrication procedure of gold nanohole arrays. The entire process comprises four steps: (a) self-assembling close-packed PS nanosphere masks on BK7 glass slides, (b) etching PS nanospheres with oxygen plasma, (c) evaporating the gold film, and (d) removing gold-coated masks by sonicating in the tetrahydrofuran solution. The SEM images for each step are also presented with a scale bar of 500 nm.

By varying the etching duration, we fabricated nanohole arrays with different hole diameters as shown in Fig. 2, and the SEM images indicate that the hole sizes were relatively consistent and well controlled by the etching process. We measured the hole diameters by averaging the diameters of all holes and listed them in Table 1. The PS nanosphere mask was successfully etched and the hole size corresponding to the nanosphere diameter gradually decreased to 233 nm as the etching duration increased to 240 s. After the gold evaporation and removal of the mask, nanohole arrays with desired parameters were fabricated and the adhesive power between the gold film and the glass substrates stabilized the whole structure to enable the following measurements for dozens of times. We plotted the hole diameter as a function of the etching duration in Fig. 2(i), showing an excellent linear relationship (R^2=0.993). It can instruct us well in the fabrication of nanohole arrays with arbitrary hole sizes under the same conditions. Furthermore, we calculated the etching rate as 0.51 nm/s based on this linear relationship, which can serve as a reference for further experiments and optimizations. The cost-effective, high-throughput, and easy-operation fabrication method is expected to improve the availability of the NSL method and promote the practical application of nanostructures.

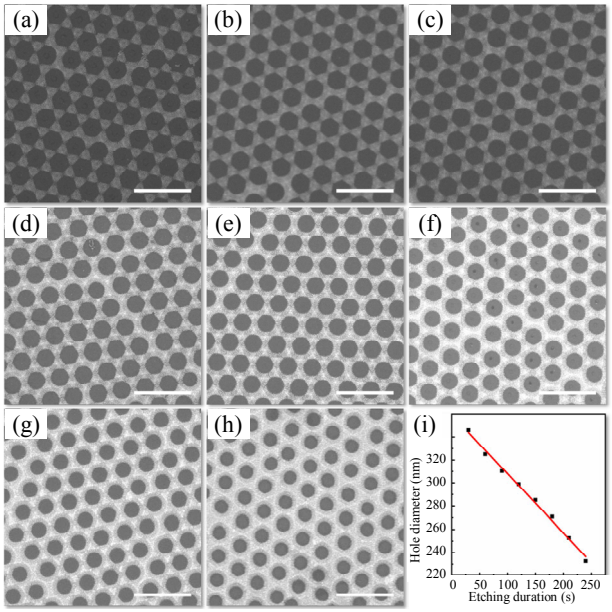

Fig. 2 Gold nanohole arrays with various hole diameters and the relationship between the hole diameter and etching duration. SEM images of gold nanohole arrays fabricated under the etching durations of (a) 30 s, (b) 60 s, (c) 90 s, (d) 120 s, (e) 150 s, (f) 180 s, (g) 210 s, and (h) 240 s; (i) nanohole diameter plotted with respect to etching duration. Scale bar: 1 μm.

Table 1 Nanohole diameters fabricated under different etching durations.

Duration (s)	30	60	90	120	150	180	210	240
Diameter (nm)	346	325	310	299	285	271	253	233

3.2 Optical properties of gold nanohole arrays

EOT occurs in metallic nanohole arrays, causing an increase in the transmitted light intensity beyond the standard aperture theory prediction. One critical analytical characteristic of metallic nanohole arrays is the wavelength shift of the EOT plasmonic band depending on the RI of the surrounding medium which is appropriate for detecting the biochemical reactions adjacent to the surface of nanohole arrays. Here, we investigated the optical properties of gold nanohole arrays with varying hole diameters using multiple parameters: the excitation wavelength, full width at half maximum (FWHM), and full height (FH)/FWHM ratio. The experimental setup is depicted in Fig. 3, where the light was vertically launched onto the nanohole arrays from the gold film side and the transmission spectra were recorded from the other side. The inset in Fig. 3 illustrates the PDMS flow cell. The lead-in and lead-out optical fibers, and the flow cell were integrated into a custom setup to ensure consistent conditions for following measurement.

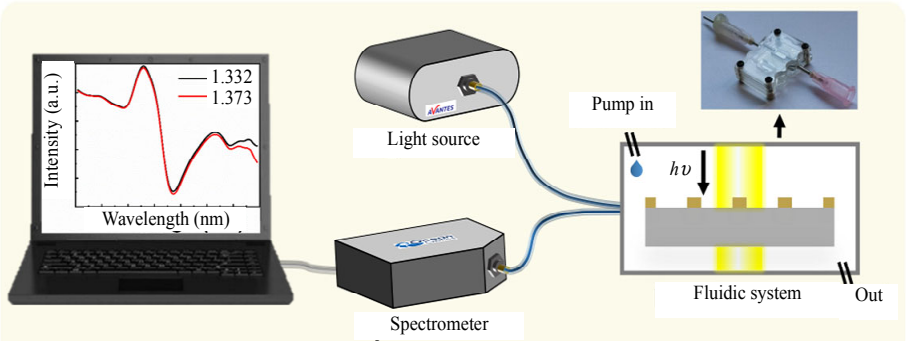

Fig. 3 Experimental setup for examining the optical properties and sensing performance of gold nanohole arrays (inset is the PDMS fluidic system).

Figure 4(a) presents the normalized experimental EOT transmission spectra of gold nanohole arrays in water with a 60% vertical offset between adjacent spectra for easier discrimination, while Fig. 4(b) shows the relative positions of the two dips and the corresponding excitation wavelengths as a function of the hole diameter. The I/I_0 was calculated as follows:

$$I / I_0 = (R - D) / (R_0 - D) \times 100\% \quad (1)$$

where R is the transmission signal in water or sodium chloride solutions, D is the dark spectrum, and R_0 is the reference spectrum. Here, the transmission signals of gold nanohole arrays with different hole sizes in air were employed as the respective reference spectrum. We demonstrated that no visible transmission minimum was observed for nanohole arrays with hole diameters larger than 299 nm, similar to triangle arrays.

However, for diameters ranging from 233 nm to 299 nm, two dips were identified near 535 nm (Dip 1) and 700 nm (Dip 2). The positions of both dips were tuned significantly depending on the nanohole diameter, while the excitation wavelengths showed a distinct blue-shift trend as the nanohole diameter increased, as shown in Fig. 4(b). For the smaller nanohole diameter of 233 nm, Dip 1 was excited at 539.7 nm and the plasmonic wavelength blue-shifted to 530.6 nm as the diameter increased to 299 nm. The intensity of this plasmonic band gradually decreased from 10.0% to 2.7%. Similarly, Dip 2 blue-shifted from 715.9 nm to 683.7 nm as the diameter increased from 233 nm to 299 nm, with the intensity of 43.9 ± 5%. The intensity of both dips varied with the nanohole diameter, becoming more intense as the diameter decreased, which improved the resolution and facilitated the precise tracking of the plasmonic wavelength. Besides, we also plotted the hole diameter as a function of the dip wavelength in Fig. 4(b), showing an approximate linear relationship which was consistent with previous studies [47, 48], and the values of R^2 for Dips 1 and 2 were 0.932 and 0.967, respectively. The values of R^2 of two dips were relatively low, which might be due to the structural defects caused by the mask defects and surface roughness caused by the equipment. In future work, we can fix this issue by using higher-quality nanospheres to obtain masks with fewer defects and performing the annealing process after the evaporation to reduce the surface roughness. Overall, this large-area periodic nanostructure provided significant insights into the application of gold nanohole arrays in nanophotonics and plasmonics, highlighting their tunability and role in improving the optical resolution.

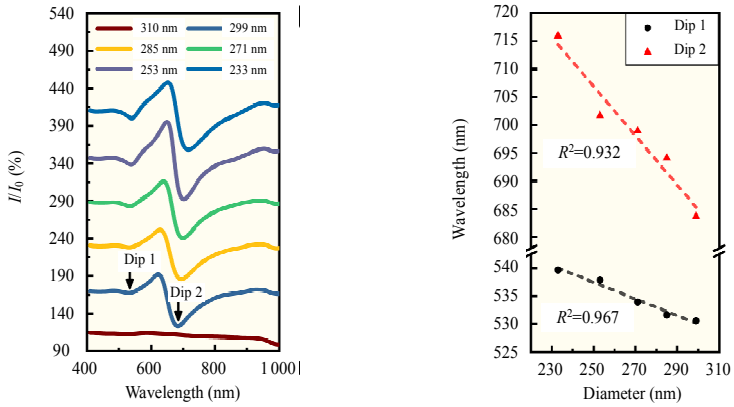

(a) (b)

Fig. 4 Optical properties of gold nanohole arrays: (a) normalized transmission spectra for gold nanohole arrays with various hole diameters in water (the adjacent transmission spectra are vertical offset by 60% for clarity) and (b) associated resonance wavelength of EOT plasmonic bands [the circles and triangles represent the wavelengths of two transmission minimums (Dip 1 and Dip 2) in spectra, respectively, and the dashed lines are obtained by linear fitting].

We also analyzed the line width of plasmonic bands in addition to their wavelength and intensity using the FWHM, as outlined in Table 2. Dip 1 had an FWHM of (37.3±5) nm, with a minimum FWHM of 32.3 nm at a diameter of 285 nm. Dip 2, on the other hand, had a significantly larger FWHM of (83.75 ± 9.75) nm, with a minimum FWHM of 74 nm at a diameter of 233 nm. In addition, the two dips showed opposite trends, with the nanohole diameter decreasing, the FWHM of Dip 1 gradually increased, while Dip 2 gradually reduced. A smaller FWHM corresponded to a narrower peak and thus better resolution of slight wavelength shifts, while a higher full height (FH) corresponded to a greater amplitude, ensuring a more reliable signal-to-noise ratio in experiments. However, the FH and FWHM tend to vary together, so they should not be considered separately. To address this, we introduced the

FH/FWHM to assess the acutance and intensity of plasmonic bands, which was the ratio of the FH (intensity-related) to FWHM (acutance-related). Dip 1 exhibited an increasing trend in the FH/FWHM with decreasing nanohole diameters, reaching a maximum of 23.6×10^{-2}%/nm at a diameter of 233 nm, while the FH/FWHM range of Dip 2 was $(53\pm11.4)\times10^{-2}$%/nm, reaching a maximum of 64.4×10^{-2}%/nm at a diameter of 253 nm. This parameter provided a reliable methodology to evaluate the plasmonic properties, with a higher FH/FWHM, indicating the better spectral resolution for plasmonic bands.

Table 2 Analytical parameters of gold nanohole arrays with different diameters.

Diameter (nm)	Wavelength (nm)		Intensity (%)		FWHM (nm)		FH/FWHM (10^{-2}%/nm)	
	Dip 1	Dip 2	Dip 1	Dip 2	Dip 1	Dip 2	Dip 1	Dip 2
299	530.6	683.7	2.7	41.6	34.7	92.6	7.8	44.9
285	531.6	694.1	2.5	38.9	32.3	93.5	7.7	41.6
271	534.0	698.9	5.0	41.9	38.0	88.7	13.2	47.2
253	537.9	701.7	8.9	48.9	41.0	75.9	21.7	64.4
233	539.7	715.9	10.0	39.7	42.3	74.0	23.6	53.6

3.3 RI sensitivity for gold nanohole arrays

To evaluate the sensing potential of plasmonic nanostructures, it is crucial to measure and calibrate the sensitivity to the bulk refractive index (RIS) of the gold nanohole arrays. The normalized transmission spectra of gold nanohole arrays with different nanohole diameters are plotted in Fig. 5, where two dips were identified and marked with cyan and orange wireframes. As expected, the wavelength and intensity of the two dips exhibited distinct RI dependence. The Dip 1 regions were enlarged as shown in the insets for better discrimination. Dip 1 exhibited a minor red-shift in the wavelength and a slight increase in the intensity as the RI increased, whereas Dip 2 showed a minor red-shift in the wavelength and a significant decrease in the intensity with increasing RI. The measured resonant wavelengths are plotted as linear fits against the RIs, showing excellent linear relationships (all R^2 values were better than 0.995), as depicted in the second row of Fig. 5. The error bars, represented by the standard deviations of three replicate experiments, indicated the good stability and repeatability of the nanostructures. The RISs corresponding to Dips 1 and 2 were obtained through the slope of linear fittings and recorded in Table 3, where it was observed that the RIS of Dip 1 was significantly larger than that of Dip 2. Dip 1 had

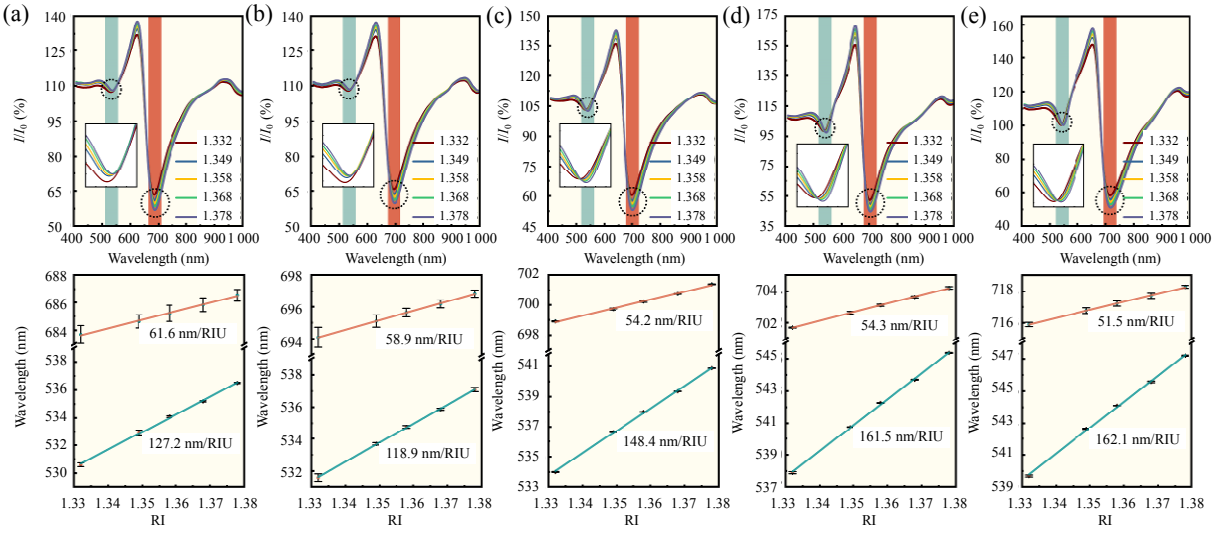

Fig. 5 Normalized transmission spectra of gold nanohole arrays of various nanohole diameters: (a) 299 nm, (b) 285 nm, (c) 271 nm, (d) 253 nm, and (e) 233 nm in NaCl solutions covering a range of RIs from 1.332 to 1.378, and the corresponding linear relationship between the measured resonant wavelengths and RIs. The plasmonic bands are highlighted by wireframes in cyan and orange, and the corresponding curves are obtained by linear fitting. The insets are the enlarged view of the Dip 1 region.

the highest RIS of 162.1 nm/RIU for a nanohole diameter of 233 nm, whereas Dip 2 reached the highest RIS of 61.6 nm/RIU for a nanohole diameter of 299 nm. The RIS of Dip 1 was highly variable for decreasing nanohole diameters and showed an increasing trend, while the RIS of Dip 2 showed a smaller variation with a decreasing trend. We could find that the RIS of our nanohole arrays did not show many advantages. However, it was important to note that the RIS of our nanohole arrays was still within the reasonable range of other reported plasmonic sensors [49]. Besides, our proposed method can also be used to fabricate novel structures for sensing applications [50, 51].

Table 3 RIS, corresponding FOM, and RI resolution of gold nanohole arrays with varied nanohole diameters.

Diameter (nm)	299		285		271		253		233	
	Dip 1	Dip 2	Dip 1	Dip 2	Dip 1	Dip 2	Dip 1	Dip 2	Dip 1	Dip 2
RIS (nm/RIU)	127.2	61.6	118.9	58.9	148.4	54.2	161.5	54.3	162.1	51.5
FOM (RIU^{-1})	3.7	0.7	3.7	0.6	3.9	0.6	3.9	0.7	3.8	0.7
RI resolution (10^{-4} RIU)	4.9	2.2	6.2	3.5	3.1	2.3	0.8	2.0	0.9	3.9

Besides the RIS, another two analytic parameters including the figure of merit (FOM) and RI resolution were also considered for practical applications, as outlined in Table 3. FOM, the ratio of RIS and FWHM, is a widely accepted performance metric for plasmonic sensors. Dip 1 had a relatively stable FOM of $(3.8\pm0.1)\ RIU^{-1}$, while Dip 2 had a smaller FOM of $(0.65\pm0.05)\ RIU^{-1}$. Higher FOM generally corresponds to lower noise and ultimately results in better limits of detection (LoD) for sensing. The RI resolution refers to the smallest RI change that can be measured in the experiment, which is calculated by dividing experimental noise by RIS and will directly affect the LoD of a sensor. Herein, both dips had the highest RI resolution of 0.8×10^{-4} RIU and 2.0×10^{-4} RIU at a diameter of 253 nm, respectively, which were comparable to other nanostructured sensors [52]. Assessing sensing potential just relying on RIS is not comprehensive, while these two parameters provide a multidimensional reference for specific sensing applications. It can be seen that the maximum FOM in this manuscript is much lower than those of some other periodic metal nanostructures. However, we would like to clarify that the maximum FOM in this manuscript is not necessarily a limitation of our method but rather a result of currently experimental conditions used. From the definition of the FOM, we can find that increasing RIS or decreasing FWHM will both improve the FOM. The RIS of nanohole arrays can be tuned by varying the period, hole diameter, hole shape, metallic composition, and the RI of the substrate [53]. And the periodicity of the nanohole arrangement has a crucial effect on the FWHM. In addition, the roughness of the surface and the nature of the nanohole wall may also affect the RIS and FWHM. In our proposed NSL method, the period could be tuned by using the nanosphere with various diameters, the hole diameter could be tuned by adjusting the etching duration, the metallic composition could be easily changed during the evaporation process, and the RI of the substrate could be directly modulated by transferring the PS monolayer to different substrates. Thus, in future work, we can further improve the FOM from the above aspects, such as using nanospheres with the larger diameter (corresponding to the larger period), employing silver as the metallic composition, selecting the substrate with the appropriate RI to get the higher RIS, using higher-quality nanospheres (corresponding to the better periodicity) to obtain the narrower linewidth, and performing annealing operations to reduce the surface roughness and modify the nature of nanohole wall. We believe that our work can serve as a foundation for future works aiming at achieving the higher RIS and FOM.

3.4 FDTD simulation

To better understand the optical properties of our nanostructure, as shown in Fig. 6, we employed FDTD simulation to calculate the transmission

spectrum of a nanohole array with the 233 nm hole diameter. Three dips were demonstrated at 550 nm (λ_0), 573 nm (λ_1), and 677 nm (λ_2) in simulation, respectively [Fig. 6(a)]. However, we only observed two dips in the experimental spectrum [Fig. 6(b)] corresponding to λ_1' and λ_2'. Then, the simulations of the transmission spectra in various RI media and the corresponding RISs for three dips were calculated by linear fitting, as shown in Fig. 6(c). It could be observed that λ_0 was insensitive to external RI changes, for it was caused by the interband transition of gold, which was associated with the reference light [54]. However, λ_1 and λ_2 were sensitive to the RI change, and the RIS for λ_1 reached a maximum of 350 nm/RIU. Compared with the experimental results, the RIS of λ_1' (162.1 nm/RIU) was significantly lower than the RIS of λ_1, and the RIS of λ_2' (51.5 nm/RIU) was consistent with that of λ_2 (50.0 nm/RIU). Accordingly, we concluded that λ_1' was degenerated from λ_0 and λ_1, and λ_2' corresponded to λ_2. Besides, the huge spectral shape difference between the experimental and simulated spectra arose from multiple factors, including the structural defects, the taper of nanohole wall, the discontinuity of the gold film, and the high surface roughness.

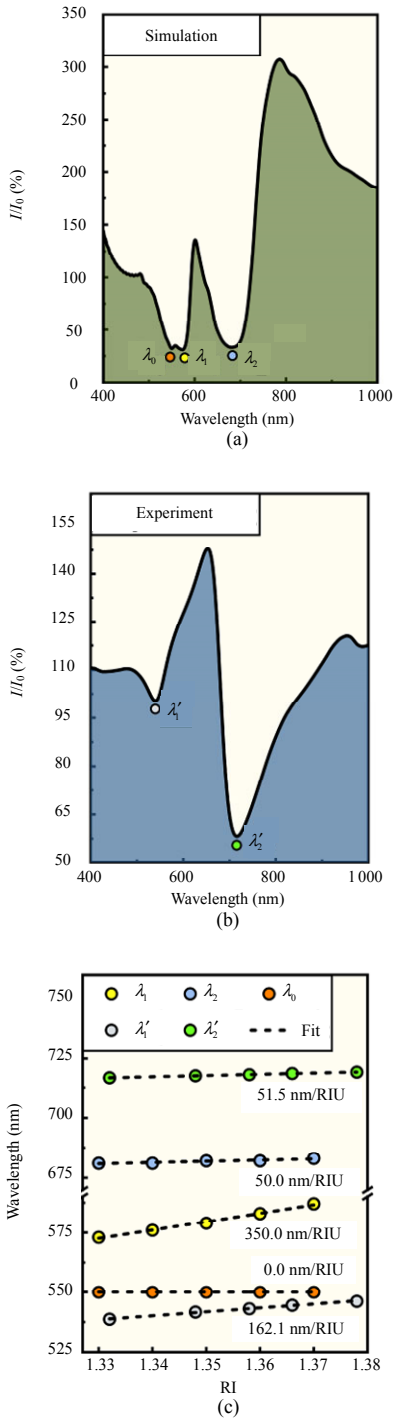

Fig. 6 Comparison between the (a) simulation and (b) experiment of the transmission spectrua of the gold nanohole array with a diameter of 233 nm in water; (c) relationship between resonant wavelengths and RIs for dips corresponds to the simulation and experiment. The dashed lines are obtained by linear fitting.

As mentioned above, the simulation results matched well with the experimental results. To further investigate the generation mechanism of λ_1 and λ_2, we simulated the electric and magnetic field distributions in *x*-*z* and *x*-*y* planes as displayed in Fig. 7. The simulation results for λ_1 [Fig. 7(a)] revealed that the electric field was mainly confined to the top surface of the nanohole array, whereas for λ_2 [Fig. 7(b)] the electric field was predominantly localized on the bottom surface, leading to the separation of two dips in transmission spectra. In addition, our analysis of the magnetic field distribution indicated that λ_1 exhibited the stronger optical energy localization at the top surface, while the energy for λ_2 was primarily concentrated at the bottom surface. Since the strength of the dip was influenced by the surrounding environment, our findings demonstrated that the higher near-field

localization at the metal-dielectric interface corresponded to the increased RIS. Notably, we found that the near-field intensity on the top surface for λ_1 was significantly greater than that of λ_2, indicating that λ_1 has a higher RIS than λ_2, which was consistent with our experimental results. The theoretical results provide a good explanation for the resonance peak degeneracy phenomenon observed in the experiment and also provide an effective reference for improving the sensing performance of the subsequent structures and regulating the position of resonance peaks.

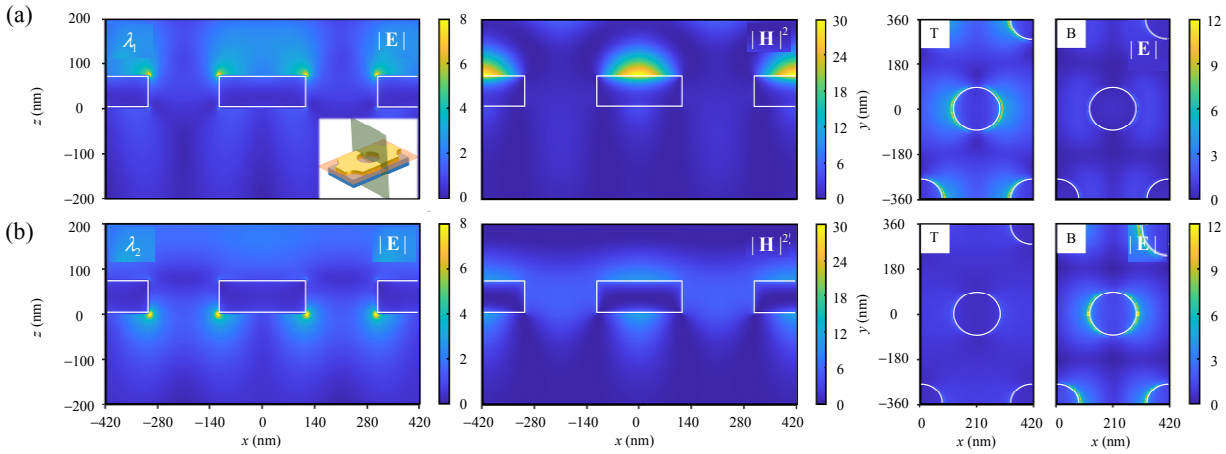

Fig. 7 FDTD simulation results for the gold nanohole array with the 233 nm hole diameter in water. The electric field |**E**| and magnetic field $|\mathbf{H}|^2$ distribution in the *x*-*z* plane and the electric field |**E**| distribution on the top (T)/bottom (B) surface in the *x*-*y* plane of the nanohole array for dips: (a) λ_1 at 573 nm and (b) λ_2 at 677 nm. The *x*-*y* and *x*-*z* planes are marked by red and green transparent rectangles, respectively, as shown in the inset of (a). In the *x*-*z* plane, the negative *z* region corresponds to the BK7 glass substrate, the rectangular wireframes are the metal regions, and the positive *z* region is filled with water. In the *x*-*y* plane, the circular wireframes are the hole regions.

4. Conclusions

In summary, we demonstrated the fabrication of large-scale (1×2 cm^2) nanohole arrays on BK7 glass substrates using a low-cost and high-throughput improved nanosphere lithography process. Hemispherical-depression-assisted self-assembly produced the high-quality templated PS monolayer resulting in highly ordered nanohole arrays. The nanohole arrays had a fixed period of 420 nm, and their hole diameters were successfully regulated from 233 nm to 346 nm through a low-cost O_2 plasma etching process. Besides, the period and diameter of nanohole arrays could be facilely tuned by using different sizes nanospheres and adjusting the etching durations. The optical properties and sensing performances were systematically investigated, revealing two transmission dips in spectra that were sensitive to changes in surrounding environments. Dip 1 exhibited a significantly larger RIS than Dip 2, reaching a maximum of 162.1 nm/RIU with a 233 nm diameter. Furthermore, the experimental results were in good agreement with FDTD simulation predictions. Our results showed that these nanohole arrays had the good sensing performance, low-cost and simple fabrication process, and large-scale highly ordered structures, thus, presenting a great opportunity to be utilized in practical applications, particularly as multiplex sensing chips. In future work, we can further improve the sensing performance by annealing operation and adjusting structural parameters.

Acknowledgment

This work was financially supported by the National Natural Science Foundation of China (Grant Nos. 62375036, 62005034, 62171076, and 61727816), Liaoning Cancer Hospital & Institute "Oncology+" Funds (Grant No. 2024-ZLKF-34),

and Fundamental Research Funds for the Central Universities (Grant No. DUT21RC(3)080).

Declarations

Conflict of Interest The authors declare that they have no competing interests.

Permissions All the included figures, tables, or text passages that have already been published elsewhere have obtained the permission from the copyright owner(s) for both the print and online format.

References

[1] P. Christopher, H. Xin, A. Marimuthu, and S. Linic, "Singular characteristics and unique chemical bond activation mechanisms of photocatalytic reactions on plasmonic nanostructures," *Nature Materials*, 2012, 11(12): 1044–1050.

[2] X. Li, W. C. H. Choy, L. Huo, F. Xie, W. E. I. Sha, B. Ding, *et al.*, "Dual plasmonic nanostructures for high performance inverted organic solar cells," *Advanced Materials*, 2012, 24(22): 3046–3052.

[3] J. Butet, P. F. Brevet, and O. J. F. Martin, "Optical second harmonic generation in plasmonic nanostructures: from fundamental principles to advanced applications," *ACS Nano*, 2015, 9(11): 10545–10562.

[4] Y. Zhao, A. N. Askarpour, L. Sun, J. Shi, X. Li, and A. Alù, "Chirality detection of enantiomers using twisted optical metamaterials," *Nature Communications*, 2017, 8(1): 14180.

[5] A. M. Shrivastav, U. Cvelbar, and I. Abdulhalim, "A comprehensive review on plasmonic-based biosensors used in viral diagnostics," *Communications Biology*, 2021, 4(1): 70.

[6] J. Zeng, Y. Zhang, T. Zeng, R. Aleisa, Z. Qiu, Y. Chen, *et al.*, "Anisotropic plasmonic nanostructures for colorimetric sensing," *Nano Today*, 2020, 32: 100855.

[7] H. Gleiter, "Nanostructured materials: basic concepts and microstructure," *Acta Materialia*, 2000, 48(1): 1–29.

[8] C. Song, B. Yang, Y. Zhu, Y. Yang, and L. Wang, "Ultrasensitive sliver nanorods array SERS sensor for mercury ions," *Biosensors and Bioelectronics*, 2017, 87: 59–65.

[9] G. A. Lopez, M. C. Estevez, M. Soler, and L. M. Lechuga, "Recent advances in nanoplasmonic biosensors: applications and lab-on-a-chip integration," *Nanophotonics*, 2017, 6(1): 123–136.

[10] D. Zopf, A. Pittner, A. Dathe, N. Grosse, A. Csáki, K. Arstila, *et al.*, "Plasmonic nanosensor array for multiplexed DNA-based pathogen detection," *ACS Sensors*, 2019, 4(2): 335–343.

[11] Y. Zhang, L. Lu, and X. Li, "Detection technologies for RNA modifications," *Experimental & Molecular Medicine*, 2022, 54(10): 1601–1616.

[12] T. Xie, Z. Cao, Y. Li, Z. Li, F. L. Zhang, Y. Gu, *et al.*, "Highly sensitive SERS substrates with multi-hot spots for on-site detection of pesticide residues," *Food Chemistry*, 2022, 381: 132208.

[13] C. Li and Y. Jin, "Shell-isolated plasmonic nanostructures for biosensing, catalysis, and advanced nanoelectronics," *Advanced Functional Materials*, 2021, 31(7): 2008031.

[14] S. Su, T. Yu, J. Hu, and Y. Xianyu, "A bio-inspired plasmonic nanosensor for angiotensin-converting enzyme through peptide-mediated assembly of gold nanoparticles," *Biosensors and Bioelectronics*, 2022, 195: 113621.

[15] X. Liu, W. Liu, and B. Yang, "Deep-elliptical-silver-nanowell arrays (d-EAgNWAs) fabricated by stretchable imprinting combining colloidal lithography: a highly sensitive plasmonic sensing platform," *Nano Research*, 2019, 12(4): 845–853.

[16] R. F. Balderas-Valadez and C. Pacholski, "Plasmonic nanohole arrays on top of porous silicon sensors: a win-win situation," *ACS Applied Materials & Interfaces*, 2021, 13(30): 36436–36444.

[17] I. Misbah, F. Zhao, and W. C. Shih, "Symmetry breaking-induced plasmonic mode splitting in coupled gold-silver alloy nanodisk array for ultrasensitive RGB colorimetric biosensing," *ACS Applied Materials & Interfaces*, 2019, 11(2): 2273–2281.

[18] I. O. Oguntoye, B. K. Simone, S. Padmanabha, G. Z. Hartfield, P. Amrollahi, T. Y. Hu, *et al.*, "Silicon nanodisk Huygens metasurfaces for portable and low-cost refractive index and biomarker sensing," *ACS Applied Nano Materials*, 2022, 5(3): 3983–3991.

[19] S. Mehla, P. R. Selvakannan, and S. K. Bhargava, "Readily tunable surface plasmon resonances in gold nanoring arrays fabricated using lateral electrodeposition," *Nanoscale*, 2022, 14(28): 9989–9996.

[20] H. Cheng, X. Dong, Y. Yang, Y. Feng, T. Wang, M. A. Tahir, *et al.*, "Au nanoring arrays as surface enhanced Raman spectroscopy substrate for chemical component study of individual atmospheric aerosol particle," *Journal of Environmental Sciences*, 2021, 100: 11–17.

[21] B. Zhou, X. Xiao, T. Liu, Y. Gao, Y. Huang, and W. Wen, "Real-time concentration monitoring in microfluidic system via plasmonic nanocrescent arrays," *Biosensors and Bioelectronics*, 2016, 77: 385–392.

[22] M. C. Giordano, A. Foti, E. Messina, P. G. Gucciardi, D. Comoretto, and F. Buatier de Mongeot, "SERS amplification from self-organized arrays of plasmonic nanocrescents," *ACS Applied Materials & Interfaces*, 2016, 8(10): 6629–6638.

[23] Y. Liu, S. H. Wu, X. Y. Du, and J. J. Sun, "Plasmonic Ag nanocube enhanced SERS biosensor for sensitive detection of oral cancer DNA based on nicking endonuclease signal amplification and heated electrode," *Sensors and Actuators B: Chemical*, 2021, 338: 129854.

[24] B. Ai, L. Wang, H. Mohwald, Y. Yu, and G. Zhang, "Asymmetric half-cone/nanohole array films with structural and directional reshaping of extraordinary optical transmission," *Nanoscale*, 2014, 6(15): 8997–9005.

[25] T. W. Ebbesen, H. J. Lezec, H. F. Ghaemi, T. Thio, and P. A. Wolff, "Extraordinary optical transmission through sub-wavelength hole arrays," *Nature*, 1998, 391(6668): 667–669.

[26] T. Rindzevicius, Y. Alaverdyan, B. Sepulveda, T. Pakizeh, M. Käll, R. Hillenbrand, *et al.*, "Nanohole plasmons in optically thin gold films," *The Journal of Physical Chemistry C*, 2007, 111(3): 1207–1212.

[27] M. P. Murray-Méthot, M. Ratel, and J. F. Masson, "Optical properties of Au, Ag, and bimetallic Au on Ag nanohole arrays," *The Journal of Physical Chemistry C*, 2010, 114(18): 8268–8275.

[28] J. H. Kang, J. H. Choe, D. S. Kim, and Q. H. Park, "Substrate effect on aperture resonances in a thin metal film," *Optics Express*, 2009, 17(18): 15652–15658.

[29] B. Du, Y. Ruan, T. T. Ly, P. Jia, Q. Sun, Q. Feng, *et al.*, "MoS_2-enhanced epoxy-based plasmonic fiber-optic sensor for selective and sensitive detection of methanol," *Sensors and Actuators B: Chemical*, 2020, 305: 127513.

[30] C. Song, X. Jiang, Y. Yang, J. Zhang, S. Larson, Y. Zhao, *et al.*, "High-sensitive assay of nucleic acid using tetrahedral DNA probes and DNA concatamers with a surface-enhanced Raman scattering/surface plasmon resonance dual-mode biosensor based on a silver nanorod-covered silver nanohole array," *ACS Applied Materials & Interfaces*, 2020, 12(28): 31242–31254.

[31] B. Ai, P. Basnet, S. Larson, W. Ingram, and Y. Zhao, "Plasmonic sensor with high figure of merit based on differential polarization spectra of elliptical nanohole array," *Nanoscale*, 2017, 9(38): 14710–14721.

[32] X. Luo, Y. Xing, D. D. Galvan, E. Zheng, P. Wu, C. Cai, *et al.*, "Plasmonic gold nanohole array for surface-enhanced Raman scattering detection of DNA methylation," *ACS Sensors*, 2019, 4(6): 1534–1542.

[33] V. Garg, R. G. Mote, and J. Fu, "Focused ion beam direct fabrication of subwavelength nanostructures on silicon for multicolor generation," *Advanced Materials Technologies*, 2018, 3(8): 1800100.

[34] H. W. Deckman and J. H. Dunsmuir, "Natural lithography," *Applied Physics Letters*, 1982, 41(4): 377–379.

[35] Y. Wang, H. B. Chong, Z. Zhang, and Y. Zhao, "Large-area fabrication of complex nanohole arrays with highly tunable plasmonic properties," *ACS Applied Materials & Interfaces*, 2020, 12(33): 37435–37443.

[36] I. G. Balasa, T. Cesca, B. Kalinic, D. Piccotti, C. Scian, and G. Mattei, "Double-Langmuir model for optimized nanohole array-based plasmonic biosensors," *Applied Surface Science*, 2021, 556: 149802.

[37] C. W. Moon, G. Kim, and J. K. Hyun, "Enhancing the plasmonic component of photonic-plasmonic resonances in self-assembled dielectric spheres on Ag," *Journal of Materials Chemistry C*, 2021, 9(5): 1764–1771.

[38] X. Fang, C. Zheng, Z. Yin, Z. Wang, J. Wang, J. Liu, *et al.*, "Hierarchically ordered silicon metastructures from improved self-assembly-based nanosphere lithography," *ACS Applied Materials & Interfaces*, 2020, 12(10): 12345–12352.

[39] Y. C. Lu and C. H. Hsueh, "Fabrication of periodic Ag tetrahedral nanopyramids via H_2O_2-assisted nanosphere lithography for plasmonic applications," *Colloids and Surfaces A: Physicochemical and Engineering Aspects*, 2021, 628: 127278.

[40] H. Zheng, Y. Zhou, C. F. Ugwu, A. Du, I. I. Kravchenko, and J. G. Valentine, "Large-scale metasurfaces based on grayscale nanosphere lithography," *ACS Photonics*, 2021, 8(6): 1824–1831.

[41] J. Guang, M. Lu, Y. Liu, R. Fan, C. Wang, R. Li, *et al.*, "Flexible and speedy preparation of large-scale polystyrene monolayer through hemispherical-depression-assisted self-assembling and vertical lifting," *ACS Applied Polymer Materials*, 2023, 5(4): 2674–2683.

[42] R. M. Pasternack, S. Rivillon Amy, and Y. J. Chabal, "Attachment of 3-(aminopropyl)triethoxysilane on silicon oxide surfaces: dependence on solution temperature," *Langmuir*, 2008, 24(22): 12963–12971.

[43] F. Hernáinz and A. Caro, "Variation of surface tension in aqueous solutions of sodium dodecyl sulfate in the flotation bath," *Colloids and Surfaces A: Physicochemical and Engineering Aspects*, 2002, 196(1): 19–24.

[44] R. L. Hoffman, "A study of the advancing interface.

I. Interface shape in liquid-gas systems," *Journal of Colloid and Interface Science*, 1975, 50(2): 228–241.

[45] P. B. Johnson and R. W. Christy, "Optical constants of the noble metals," *Physical Review B*, 1972, 6(12): 4370–4379.

[46] J. Henson, E. Dimakis, J. DiMaria, R. Li, S. Minissale, L. Dal Negro, *et al.*, "Enhanced near-green light emission from InGaN quantum wells by use of tunable plasmonic resonances in silver nanoparticle arrays," *Optics Express*, 2010, 18(20): 21322–21329.

[47] T. Ohno, C. Wadell, S. Inagaki, J. Shi, Y. Nakamura, S. Matsushita, *et al.*, "Hole-size tuning and sensing performance of hexagonal plasmonic nanohole arrays," *Optical Materials Express*, 2016, 6(5): 1594–1603.

[48] C. Valsecchi, L. E. Gomez Armas, and J. Weber de Menezes, "Large area nanohole arrays for sensing fabricated by interference lithography," *Sensors (Basel)*, 2019, 19(9): 2182.

[49] H. Kurt, P. Pishva, Z. S. Pehlivan, E. G. Arsoy, Q. Saleem, M. K. Bayazıt, *et al.*, "Nanoplasmonic biosensors: theory, structure, design, and review of recent applications," *Analytica Chimica Acta*, 2021, 1185: 338842.

[50] F. Xu, J. Ma, K. Hu, Z. Zhang, C. Ma, B. O. Guan, *et al.*, "Ultrahigh sensitivity of hydrogen detection with a perforated Pd film on a miniature fiber tip," *Sensors and Actuators B: Chemical*, 2024, 400: 134875.

[51] B. Du, Y. Ruan, D. Yang, P. Jia, S. Gao, Y. Wang, *et al.*, "Freestanding metal nanohole array for high-performance applications," *Photonics Research*, 2020, 8(11): 1749–1756.

[52] S. Nair, C. Escobedo, and R. G. Sabat, "Crossed surface relief gratings as nanoplasmonic biosensors," *ACS Sensors*, 2017, 2(3): 379–385.

[53] Z. Zhang, F. Zhao, R. Gao, C. Y. Jao, C. Ma, J. Li, *et al.*, "Rayleigh anomaly-enabled mode hybridization in gold nanohole arrays by scalable colloidal lithography for highly-sensitive biosensing," *Nanophotonics*, 2022, 11(3): 507–517.

[54] Y. Liang, Z. Yu, L. Li, and T. Xu, "A self-assembled plasmonic optical fiber nanoprobe for label-free biosensing," *Scientific Reports*, 2019, 9(1): 7379.